

Check for updates

Geometrically Templated, Ultra-Lightweight and High Strength Soap Films from Lyotropic Liquid Crystalline **Graphene Oxide/Polymer Composites**

Yinding Chi, Yuchong Gao, Mostafa Akbari, Kun-Hao Yu, Kun-Yu Wang, Mohit Patel, Shouhong Fan, Ziyun Zhang, Masoud Akbarzadeh, and Shu Yang*

Cellular solids composed of a network of interconnected pores offer low-density and high strength-to-weight ratio as exemplified by wood, bones, corks, and shells. However, the slender edges and low connectivity of the structs in cellular lattices make them vulnerable to buckle, fracture, or collapse. Here, by taking advantage of the continuity of a thin film that can follow curvatures and dissipate energy, shellular materials are created by dip coating a wireframe of the primitive triply periodic minimal surface (TPMS) with an aqueous solution of lyotropic liquid crystalline graphene oxide (GO)/polymer composites. Regulated by surface tension, GO nanosheets align on the polymer soap film as the stress builds up during drying. When the wireframe mesh density is low, the shellular material is film-dominated, demonstrating superior mechanical strength (384.30 Nm kg⁻¹) and high specific energy absorption (1.59 kJ kg⁻¹) yet lightweight (equivalent density, 0.063 g cm⁻³), with an energy absorption rate comparable to that of carbon nanotube-based lattices but a lower equivalent density. The study offers insights into designing lightweight yet highstrength structural materials that also function as impact energy absorbers.

1. Introduction

Cellular structures consisting of periodically interconnected pores, including honeycombs, strut-based Kelvin lattices, and

Y. Chi, Y. Gao, K.-H. Yu, K.-Y. Wang, M. Patel, S. Fan, Z. Zhang, S. Yang Department of Materials Science and Engineering University of Pennsylvania

3231 Walnut Street, Philadelphia, PA 19104, United States

E-mail: shuyang@seas.upenn.edu

M. Akbari, M. Akbarzadeh Polyhedral Structures Laboratory Department of Architecture Stuart Weitzman School of Design University of Pennsylvania Philadelphia, PA 19146, United States

The ORCID identification number(s) for the author(s) of this article can be found under https://doi.org/10.1002/adfm.202512357

© 2025 The Author(s). Advanced Functional Materials published by Wiley-VCH GmbH. This is an open access article under the terms of the Creative Commons Attribution License, which permits use, distribution and reproduction in any medium, provided the original work is properly

DOI: 10.1002/adfm.202512357

triply periodic minimal surfaces (TPMS), have been observed in wood, bones, butterfly wings, and sea urchins[1,2] to provide unique mechanical properties, including high strength, high stiffness-to-weight ratio, large surface area-to-volume ratio, and superior mechanical energy absorption while being lightweight. In particular, TPMS structures with minimal surfaces repeated periodically in 3D and zero mean curvature at each point on the surface^[3,4] are promising structural building blocks with isotropic mechanical properties and minimal bending energy.[5] When strutbased cellular architectures are converged into thin sheets, shell-based (shellular) cells are formed, which can distribute load and heat effectively.[6] While TPMS cellular structures show a bending-dominated behavior, the shellular structures are nearly stretching-dominated, showing the loadbearing capacity three times that of the cellular counterpart.[7] Therefore, they are

ideal sustainable structural materials^[8] that can reduce material waste, costs, and environmental impact without compromising structural performance. However, fabricating ultrathin wall TPMS shellular structures with smooth and continuous curvatures is challenging with the conventional additive manufacturing methods, though layer-by-layer stacking, [9] as it will bear random defects, nor be energy efficient.

Meanwhile, the intrinsic material composition and alignment are crucial to mechanical performance. Compared with polymers and metals, carbon-based anisotropic nanomaterials such as carbon nanotubes (CNTs),[10] graphene, and graphene oxide (GO) nanosheets[11] offer exotic and anisotropic electrical, thermal, and mechanical properties. When assembled and aligned in liquid crystal (LC) phases, which blend the fluidity of a liquid with the long-range order of a crystal, GO nanosheets offer the potential to direct energy dissipation.^[12] When dispersed in water, GO nanosheets can form the lyotropic LC (LLC) phase above a critical concentration, [13,14] where interactions such as $\pi - \pi$ stacking, electrostatic repulsion, and hydrogen bonding could contribute to the long-range ordering of the nanosheets to maximize the translational entropy of the system. Such preordering in LLC phases is a prerequisite to aligning GO nanosheets through external stimuli.[13]

16163028, 0, Downloaded from https://advanced.onlinelibrary.wiley.com/doi/10.1002/adfm.202512357 by University Of Pennsylvania, Wiley Online Library on [22/09/2025]. See the Terms and Conditions (https://onlinelibrary.wiley.com/term/terms/files/com/terms

and-conditions) on Wiley Online Library for rules of use; OA articles are governed by the applicable Creative Commons-

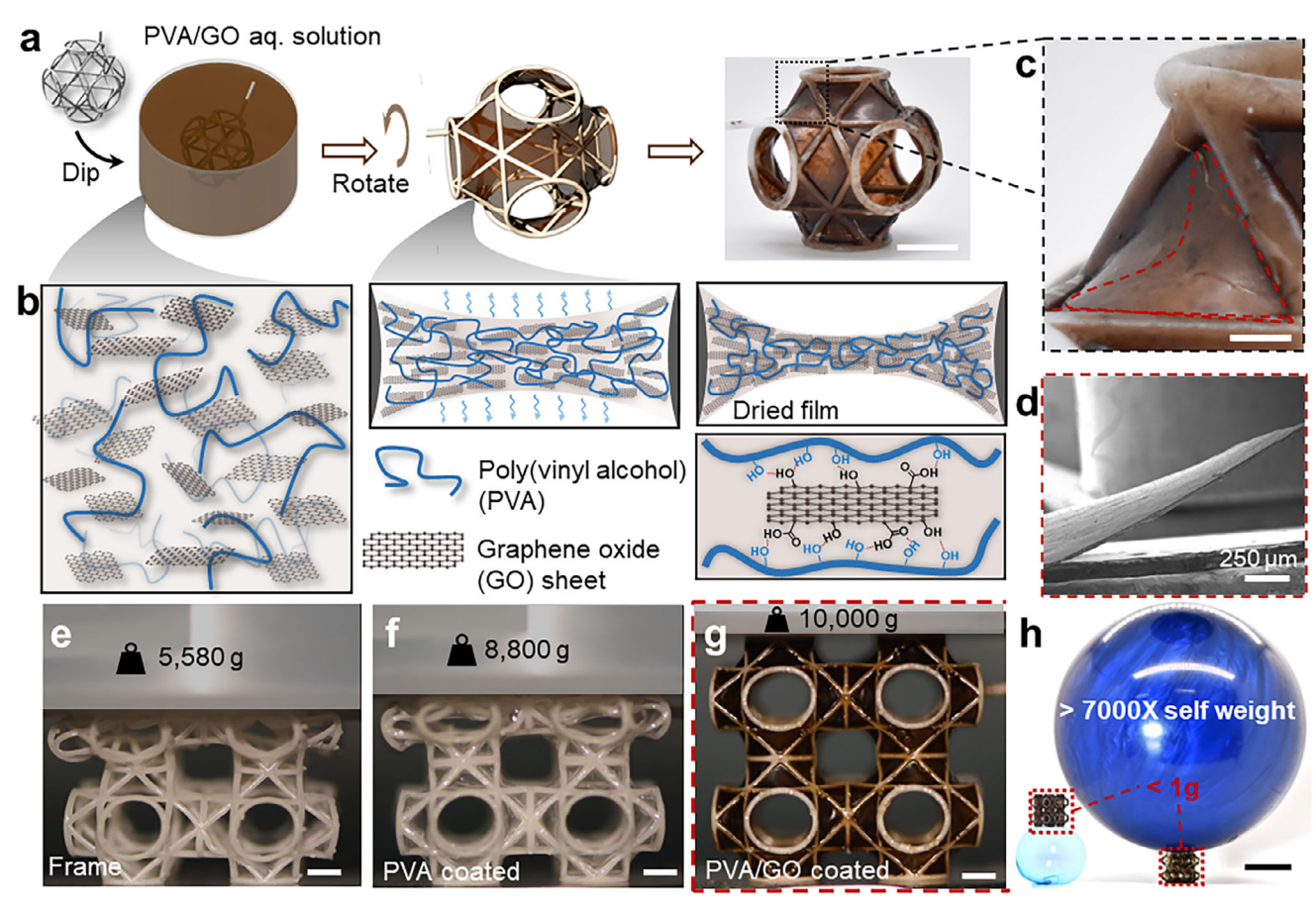


Figure 1. Preparation of PVA/GO soap film-coated P surfaces. a,b) Schematic illustrations of the dip-coating fabrication of a PVA/GO coated shellular P surface (a) and the corresponding assembly of GO nanosheets during the drying process (b). Scale bar: 5 mm. c) Zoom-in view of the curved and smooth PVA/GO soap film coated on the frame. Scale bar: 1 mm. d) Side-view SEM image of the dried PVA/GO film peeled off from the diamond-shaped frame, showing a continuous curvature. e–g) Comparison of the loading bearing capabilities of 2 × 2 Schwarz P surfaces with and without coating of PVA and PVA/GO soap films, respectively. Scale bars: 5 mm. h) Photos of an ultralightweight 2 × 2 P surface coated with PVA/GO soap films sitting on a plastic balloon made from PVAc and supporting a bowling ball. Scale bar: 5 cm.

Inspired by the soap bubble formation process on a wireframe, we present a facile and defect-tolerant strategy to fabricate the shellular Schwarz primitive (P) surfaces composed of poly(vinyl alcohol) (PVA)/GO composites via a one-step dip coating of a 3D printed wireframe of P surface. Leveraging surface tension effects, the shellular structures spontaneously form smooth, curved shells conforming to minimal-energy geometries defined by the wireframe. During the evaporationinduced liquid-to-solid transition, GO nanosheets orient directionally along gradients in the evaporation rate, guided by the geometry of the polygonal boundaries. By tuning the mesh density, the mechanical response can be programmed from frame-dominated to film-dominated behaviors, enabling control over stiffness, strength, and toughness. Notably, with the lowest mesh density applied to a diamond-triangular P surface, the resulting PVA/GO shellular TPMS composites exhibit exceptional mechanical performance—combining high stiffness, strength, toughness, and energy absorption—while being ultralightweight. We further demonstrate a proof-of-concept application of these metastructures as energy-absorbing components,

such as car bumpers, effectively mitigating impact forces during collisions.

2. Results and Discussion

2.1. Design of P Surfaces Composed of PVA/GO Soap Films

The PVA/GO shellular materials are fabricated by dip coating the 3D printed wireframes from an aqueous solution of PVA and GO nanosheets (**Figure 1a**), leading to a defect-tolerant, smooth, and continuous thin shell on the strut-based template. During the drying process, the soap film adopts the minimal surface where the surface tension regulates the film to reach its minimal energy state for a given boundary constraint. To prevent the burst of the film during evaporation, we prepare the aqueous solutions from the long-chain PVA (the weight-average molecular weight, $\rm M_W \approx 1~25~000~g~mol^{-1}$ with a radius of gyration $\approx \! 27~nm^{[15]}$), which can entangle with each other to stabilize the film and tolerate defects at the molecular level[16] (Figure 1b). The GO nanosheets are dispersed in the PVA aqueous solution (20 mg mL $^{-1}$),





www.afm-journal.de

forming an LLC phase (Figure S1a,b, Supporting Information). To eliminate the effect of gravitational drainage and evenly spread the solution between the frames, the soap film-coated Schwarz P surface is slowly rotated (≈5 rpm) around a horizontal axis during the liquid-to-solid phase transition. As water evaporates, the soap film coated on the strut-based frame becomes thinner, and the stress builds up due to the osmotic pressure at two liquid-air interfaces of the freestanding film. In addition, GO nanosheets follow the stress built up during drying (Figure 1b). We note that the preordering of GO sheets into the LLC phase is critical, which facilitates the drying-induced orientation of GO sheets in the direction perpendicular to the shear force to minimize the elastic distortion energy.[17] Moreover, oxygen-containing groups on the surface of GO nanosheets are known to form strong hydrogen bonds with PVA chains.[18] Unlike the porous elastic film that evolves on the liquid substrate, [19] the suspended soap film has two liquid-to-air interfaces. The double-sided evaporation allows the GO nanosheets (lateral size ≈1 µm, thickness ≈10 nm, Figure S1c,d, Supporting Information) to assemble in a compact stacking architecture at a low relative humidity (RH, \approx 10%). After fully drying, the continuous thin film (\approx 15 μ m, measured in the center as seen from the scanning electron microscopy, SEM, image in Figure 1d) generated across the wireframe regains a curved minimal surface (Figure 1c). Such stiffening through the surface tension-regulated shear-assembly can significantly enhance the load-bearing capability: the 2×2 array of PVA/GO coated P surface (1g) can support a weight of 10 kg (≈10 000 times of its own weight), compared to a weight of 8 kg by the 2×2 array of PVA coated P surface and a weight of 5 kg by the 2×2 array of strutbased P surface without any coating. Importantly, the coating of soap films also makes P surfaces tougher, while the PVA-coated P surface and the bare wireframe fail to support 8.80 kg and 5.58 kg weights, respectively (Figure 1e-g). When it is placed on a malleable plastic balloon (≈1g, Figure S2, Supporting Information) made from polyvinyl acetate (PVAc), no deformation of the latter is observed. In contrast, it can withhold a 7 kg (≈7000 times its own weight) bowling ball on top (Figure 1h).

We note here that the soap film thickness is a function of the respective concentrations of PVA and GO, the molecular weight of PVA, the initial mass of the aqueous solution, the drying rate, and the relative humidity vs. the wireframe size. Detailed studies of these effects on PVA soap film coating can be found in a separate report.^[20] While exploring the correlation between film thickness variations and mechanical properties is certainly of interest, such an investigation would require careful tuning of multiple parameters, and drying is a dynamic process; that is, any change of the parameters could introduce variations in sample fabrication. Therefore, we focus on the investigation of the thinnest achievable film thickness (≈15 µm) in order to minimize the relative density of our P surfaces.

2.2. Alignment of the PVA/GO Soap Films Driven by Surface Tension

To further investigate the load bearing mechanism and its relationship with the alignment of GO nanosheets, we choose an equilateral triangle-shaped strut-based wireframe (side length l =20 mm, diameter of strut d = 2 mm, Figure 2a) as the platform, followed by dip coating of 40 mg PVA/GO aqueous solution (10 wt.%, PVA: GO LLCs = 10:1 w/w). Without further notice, these are the parameters used in our fabrications. The PVA/GO soap film suspended on the frame forms a catenary curve, which is thinnest at the film center and gradually thickens and pins on the frame due to the balance of surface tension and osmotic pressure differences (Figure 1b). As water evaporates, the thickness gradient is amplified, leading to the nonuniform drying rates across the in-plane and out-of-plane directions of the soap film. The inplane compressive stress continues to build and is regulated by the geometry of the frame.

To understand how GO nanosheets would align on the soap film depending on the frame geometry, we image the center and the edge of the dried PVA/GO soap film by SEM (Figure 2b). During drying of the PVA soap films suspended on a wireframe, highly ordered micro-wrinkles are formed perpendicular to the angle bisector, as a result of evaporation-induced shrinkage of the PVA films.^[20] In the case of drying the PVA/GO soap films, only shallow undulations of the stacked GO nanosheets are found near the edges of the template, which propagate along the bisector lines between the adjacent edges (wavelength $\lambda \approx 40 \, \mu m$, amplitude $A \approx 2.9 \,\mu\text{m}$, Figure 2b(i); Figure S3a,b, Supporting Information). Clearly, the directional stacking and wrinkling of the GO nanosheets originate from mechanical stress generated in the peripheral regions. In contrast, the center area shrinks uniformly without boundary constraints, leading to a crumbled surface texture (Figure 2c(i); Figure S3c,d, Supporting Information). To investigate how the boundary confinement affects an elastic sheet with a gradient thickness profile, we perform a qualitative finite element analysis (FEA), assuming the PVA/GO soap film has a thermal expansion coefficient ($\alpha = -0.2$ °C). Because the edges are fixed and cannot contract, the maximum principal stress orients normal to the bisector lines around the three corners. In contrast, the stress is randomly oriented in the center, as the film shrinks uniformly (Figure 2d). The GO nanosheets in the LLC phase orient and align along the direction of the stress generated as a result of the evaporation-induced shrinkage, depending on geometric boundary conditions.

Moreover, we utilize the polarized Raman spectroscopy to quantitatively determine the spatial orientation of GO LLCs (see Materials and Methods for details). As indicated in the literature,[21] a generalized spherical expanded harmonics orientation distribution function (ODF) can be utilized to quantify the spatial orientation of GO sheets (see the experimental setup shown in Figure 3a). At the corner regions, the laser propagates parallel to the surface of the triangular PVA/GO soap film. The intensity of Raman 2D band I_{2D} shows a strong dependence on the sample rotating to different angles Φ_x , relative to the horizontal *X* axis of the soap film, where the maximum and minimum intensity occur at $\Phi_X = 0^\circ$ and 90° , respectively (Figure 3b), indicating the lamella stacking of GOs along the thickness direction. In contrast, when the laser point is perpendicular to the surface of the PVA/GO soap film, I_{2D} is independent of the rotating angle Φ_Z (Figure 3c). We note that at the center, I_{2D} variation with the laser beam parallel to the cross-sectional direction does not strictly follow the ordered distribution, which can be attributed to the highly random surface crumbles (Figure 2c and Figure 3b,d).

To visualize the evolution of the stress-induced alignment of GO LLCs within the PVA/GO soap film during the liquid-to-solid

16163028, 0, Downloaded from https://advanced.onlinelibrary.wiley.com/doi/10.1002/adfm.202512357 by University Of Pennsylvania, Wiley Online Library on [22/09/2025]. See the Terms and Conditions (https://onlinelibrary.wiley

conditions) on Wiley Online Library for rules of use; OA articles are governed by the applicable Creative Commons I

SCIENCE NEWS

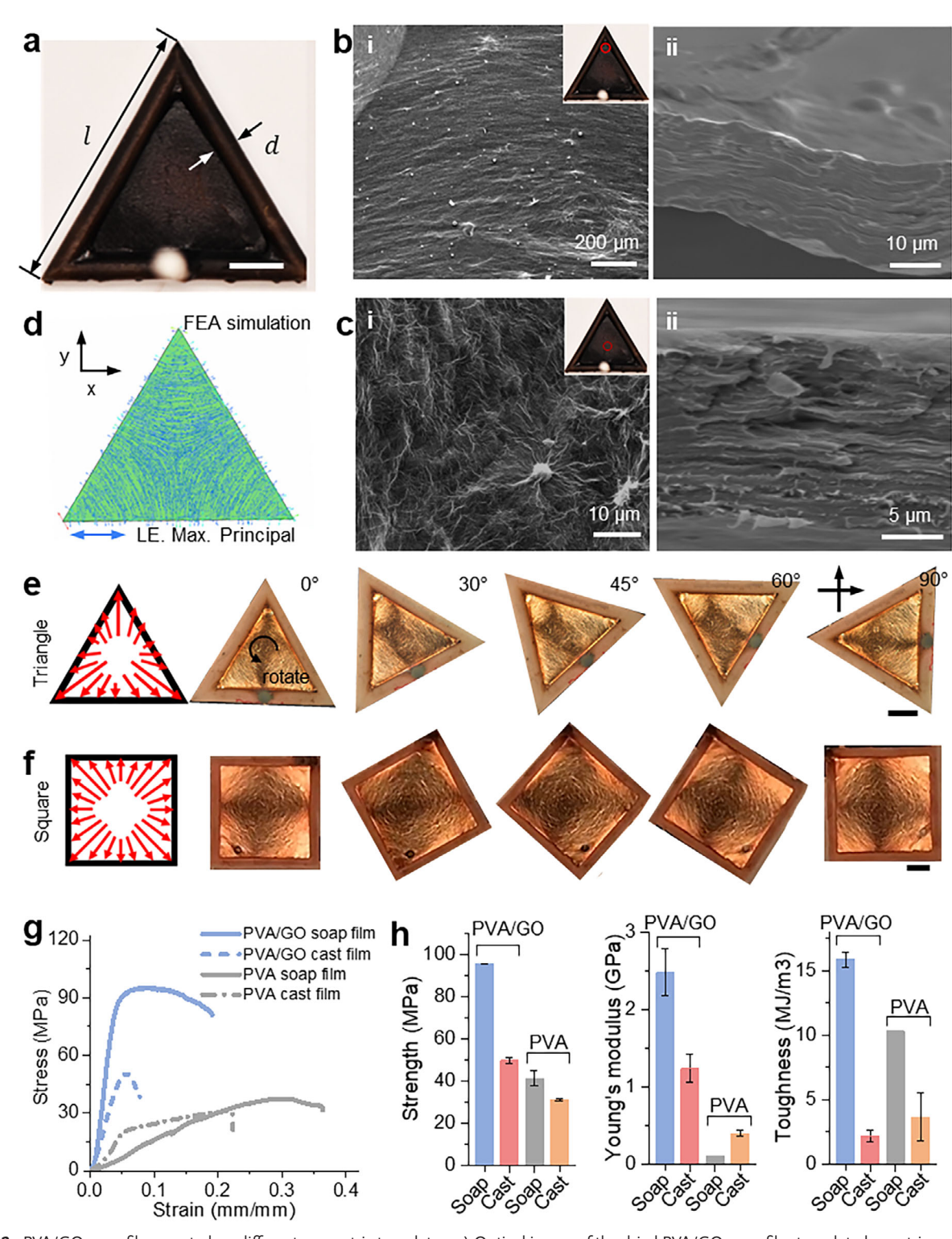


Figure 2. PVA/GO soap films coated on different geometric templates. a) Optical image of the dried PVA/GO soap film templated on a triangular strutbased frame. Side length l=20 mm, diameter d=2 mm, coating mass 40 mg, RH = 10%. Scale bar: 4 mm. b,c) SEM images of the dried PVA/GO soap film near the vertex of a triangular template (b) with top (i) and cross-sectional (ii) view; and at the center region (c) with top (i) and cross-sectional (ii) view. d) FEA result of tensile stress distribution in the soap film. Blue arrows denote the orientations of the maximum principal stress and are parallel to the alignment directions of GO LLCs. e,f) POM images showing varying birefringence of the dried triangular (e) and square-shaped (f) PVA/GO soap films as the films rotate relative to the two cross polarizers at angles of 0°, 30°, 45°, 60°, and 90°, respectively. Scale bars: 4 mm. g) Tensile stress—strain curves of PVA/GO and PVA soap or cast films, respectively. The soap films are templated on a square-shaped strut-based frame. h), Strength, Young's modulus, and toughness of the PVA/GO and PVA soap films vs. the cast films. Error bars represent the standard deviation from three independent samples.

16163028, 0, Downloaded from https://advanced

onlinelibrary.wiley.com/doi/10.1002/adfm.202512357 by University Of Pennsylvania, Wiley Online Library on [22/09/2025]. See the Terms and Condition

onditions) on Wiley Online Library for rules of use; OA articles are governed by the applicable Creative Commons

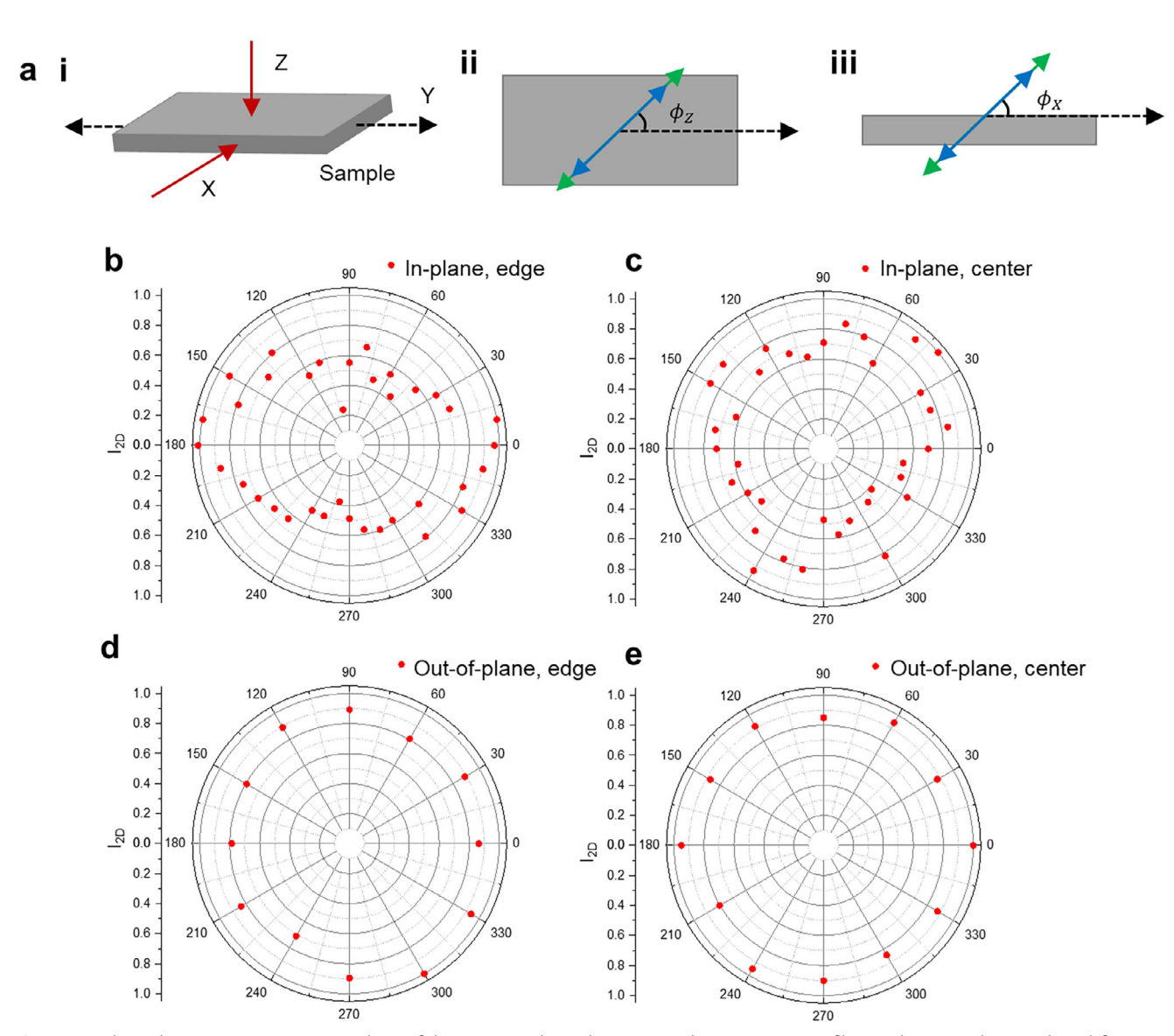


Figure 3. Polarized Raman spectroscopy analysis of the GO nanosheet alignment in the PVA/GO soap film on the triangular strut-based frame. a) Schematic of the PVA/GO film sample and polarization arrangements in Raman spectroscopy. (i) Sample in the Cartesian coordinate system. (ii and iii), VV polarization with the laser beam along the Z or X axis. The red arrow denotes laser propagation; the purple and green arrows show the incident and scattered polarizations, respectively; the dashed arrow indicates the Y direction. b,c) Relative intensities I_{2D} vary with the laser beam parallel to the in-plane direction of the triangular PVA/GO soap film at the edge (b) and center (c) regions as a function of polarized angles. d,e) Relative intensities 120 vary with the laser beam parallel to the out-of-plane direction of the triangular PVA/GO soap film at the edge (d) and center (e) regions as a function of polarized angles.

phase transition, we customize a polarized optical microscopy (POM) setup. As the sample rotates relatively to the crossed polarizers (Figure S4, Supporting Information), the birefringence also varies, confirming the alignment of GO sheets along the propagation directions of the ordered wrinkles. In contrast, the film remains dark in the center regardless of the orientation of the crossed polarizers, confirming the random arrangement of PVA chains and GO sheets (Figure 2e). When the geometry of the template is altered from triangle to square, the brightness evolves at four corners with the GO nanosheets ordered normal to the bisector lines, while the center region with random orientation

remains dark (Figure 2f). Since the stress is generated during drying, the alignment of GO nanosheets can be altered by environmental conditions (Figure S5, Supporting Information). As RH increases, the center region without birefringence grows, and GO sheets are randomly oriented (Video S1, Supporting Information). To track the spatiotemporal GO alignment process during the liquid-to-solid phase transition, we set RH 50% to monitor the stress build-up. Despite the fabrication imperfections at one corner, we observe the darkness at the center and bright patterns (ordered wrinkles) around two other corners (Figure S6 and Video **S2**, Supporting Information).





www.afm-journal.de

2.3. PVA/GO Soap Films Coated on Different Geometric Templates

Next, a library of PVA/GO soap films (mass ≈40 mg) is coated on different polygonal strut-based frames. Like those on a triangular frame, GO sheets orient perpendicular to the angle bisector around the sharp corners of the polygons, leaving a disordered center region due to competing stresses in all directions. As the polygon's vertices change from the pentagon to the octagon, the boundary effect is diminished, leading to the random orientation across the film (Figure S7a-d, Supporting Information). Meanwhile, radial symmetry of the circular wire frame drives randomly oriented GO nanosheets (Figure S7e, Supporting Information). In a negatively curved hexagonal frame (Figure S7f, Supporting Information), the local curvature promotes sheet rotation and closer conformation to the curved surface, diminishing boundary effects and yielding more aligned GO sheets around vertices compared to those on a planar hexagon (Figure S7b, Supporting Information). To verify the correlation between the alignment of GO nanosheets and the surface texture of the soap film, we incorporate a rotatable waveplate in the POM setup. The slow axis of the λ plate (630–740 nm) helps to identify the local director of the GO sheets. As a positive birefringent material, PVA shows a blueshift when aligned with the waveplate's slow axis or a redshift when aligned perpendicularly. Conversely, GO, a negatively birefringent material, exhibits a redshift when aligned. By comparing POM images of PVA and PVA/GO films with the waveplate, we confirm that the alignment of LLC GO sheets matches the wrinkles generated in the PVA soap film coated on the template (Figure \$4b, Supporting Information).

Next, we evaluate the mechanical properties of the PVA/GO and PVA soap films coated on the square-shaped frame, as other polygons are more difficult to conduct the tensile tests (Figure 2g). Films are also cast on a substrate as controls. The Young's modulus (2.47 GPa) and strength (95 MPa) of the PVA/GO soap film outperform those of the PVA/GO cast film (1.23 GPa, 49 MPa), the PVA soap film (0.10 GPa, 41 MPa), and the PVA cast film (0.39 GPa, 31 MPa), attributed to GO's intrinsic stiffness (380–470 $GPa^{[22]}$). The toughness of the PVA/GO soap film (15 MJ m⁻³) is 7 times larger than that of the cast film, 2.1 MJ $\,\mathrm{m}^{-3}$ (Figure 2h). These imply that the GO nanosheets can efficiently dissipate the elastic energy by reorienting themselves to mitigate the stress, thus preventing crack formation and enhancing the mechanical properties. [23] Interestingly, the PVA soap film has a lower Young's modulus (0.10 GPa) but higher strength (41 MPa) and toughness (10.3 MJ m⁻³) compared to its isotropic counterpart, the cast film, exhibiting increased flexibility, reduced in-plane stiffness, and anisotropic mechanical response due to the macroscopic crumbling of the film.

2.4. Soap Film Coated P Surfaces with Tunable Mechanical Properties

Next, we evaluate the parameters that could affect the mechanical properties of the shellular structures. Utilizing methods of polyhedral graphic statics (PGS),^[7] we design and 3D print a Diamond Triangle (DT)-based Schwarz P surface^[24] as a template to coat the PVA/GO soap film (**Figure 4a**). Like the align-

ment observed on the soap film-coated planar triangular wireframe, GO nanosheets are also aligned on the PVA/GO-coated DT strut-based P surface (Figure S8 and Video S3, Supporting Information). We conduct compression tests on such surfaces and compare the resulting mechanical properties (normalized by total mass) with those of the control samples, including PVA soap film-coated and bare wireframe of the P surfaces (Figure 4a,b; Video \$4, Supporting Information). The results show that the specific strength (322 Nm kg⁻¹) and toughness (124 J kg⁻¹) of the PVA/GO soap film coated P surface are 2 times higher than the two controls, where PVA coated P surface shows similar performance (176 Nm kg⁻¹, 65 J kg⁻¹) as the bare strut-based structure (153 Nm kg⁻¹, or 56 J kg⁻¹) (Figure 4c). The superior mechanical performance of the shellular structures can be attributed to a combination of geometry-induced deformation, thin-film mechanics, and intrinsic anisotropy of GO nanosheets and their specific alignment within the soap films. Under loading, the ultrathin PVA/GO-coated surfaces undergo controlled stretching, buckling, and post-buckling deformation. The minimal surface topology promotes uniform stress distribution and delays localized failure. Additionally, surface tension during fabrication induces in-plane alignment of GO nanosheets, enhancing load transfer and improving stiffness, strength, and toughness.

Since soap film coating is driven by surface tension during solvent drying, when the side length of the wireframe is larger than 30 mm, the formation of soap films will be affected by gravity, leading to film rupture during drying. Therefore, to study how the soap film coating alters the mechanical strength of P surface, we keep the effective density ($\rho = 0.0246 \text{ g cm}^{-3}$) and volume $(V = 15.625 \text{ cm}^3)$ of the strut-based P surface constant, then design a library of strut-based subdivisions including DT, polyhedral and triangulated P surface with different mesh densities as soap film coated platform for further comparison (see insets of Figure 4d-f). The compression test results show that the triangulated subdivision with the highest mesh density (6.84 mm⁻²) has the highest specific compressive strength (184 Nm kgstiffness (1.13 kNm kg⁻¹), and toughness (80 J kg⁻¹) over DT (153 Nm kg^{-1} , 0.94 kNm kg^{-1} , 56 J kg^{-1} for specific compressive strength, stiffness and toughness, respectively) and polyhedral subdivisions (140 Nm kg⁻¹, 1.12 kNm kg⁻¹, 54 J kg⁻¹) without soap film coating (Figure 4g-i; Figure S9, Supporting Information). In contrast, coating with PVA/GO soap films, the specific compressive strength (384 Nm kg⁻¹), stiffness (3.47 kN kg⁻¹), and toughness (124 J kg⁻¹) of the DT frame (Weight of frame over total weight $W_{\it frame}/W_{\it total}=0.61$) are 1.5 times larger than the polyhedral $(W_{frame}/W_{total} = 0.79)$ and triangulated (W_{frame}/W_{total}) = 0.90) subdivisions, whereas there is no enhancement for PVA soap film coated subdivisions. This is because when the mesh density is high (1.45 and 6.84 mm⁻² for polyhedral and triangulated P surfaces, respectively), the area of each unit's soap film coating is very small, thus the soap film cannot redistribute the load effectively. Conversely, when the mesh density is low (0.38 mm⁻² for the DT P surface), the area of soap film per unit is large; thus, it can effectively redistribute the load through the anisotropic alignment of GO sheets. Keeping the overall volume constant, the change in mesh density alters the size of the soap film coated on each unit. Our results show that sparser meshes with larger-sized individual soap films exhibit better mechanical properties. By tuning W_{frame}/W_{total} , as the possessed area

16163028, 0, Downloaded from https://advanced.onlinelibrary.wiley.com/doi/10.1002/adfm.202512357 by University Of Pennsylvania, Wiley Online Library on [22/09/2025]. See the Terms and Conditions (https://onlinelibrary.wiley

onditions) on Wiley Online Library for rules of use; OA articles are governed by the applicable Creative Commons

CIENCE NEWS

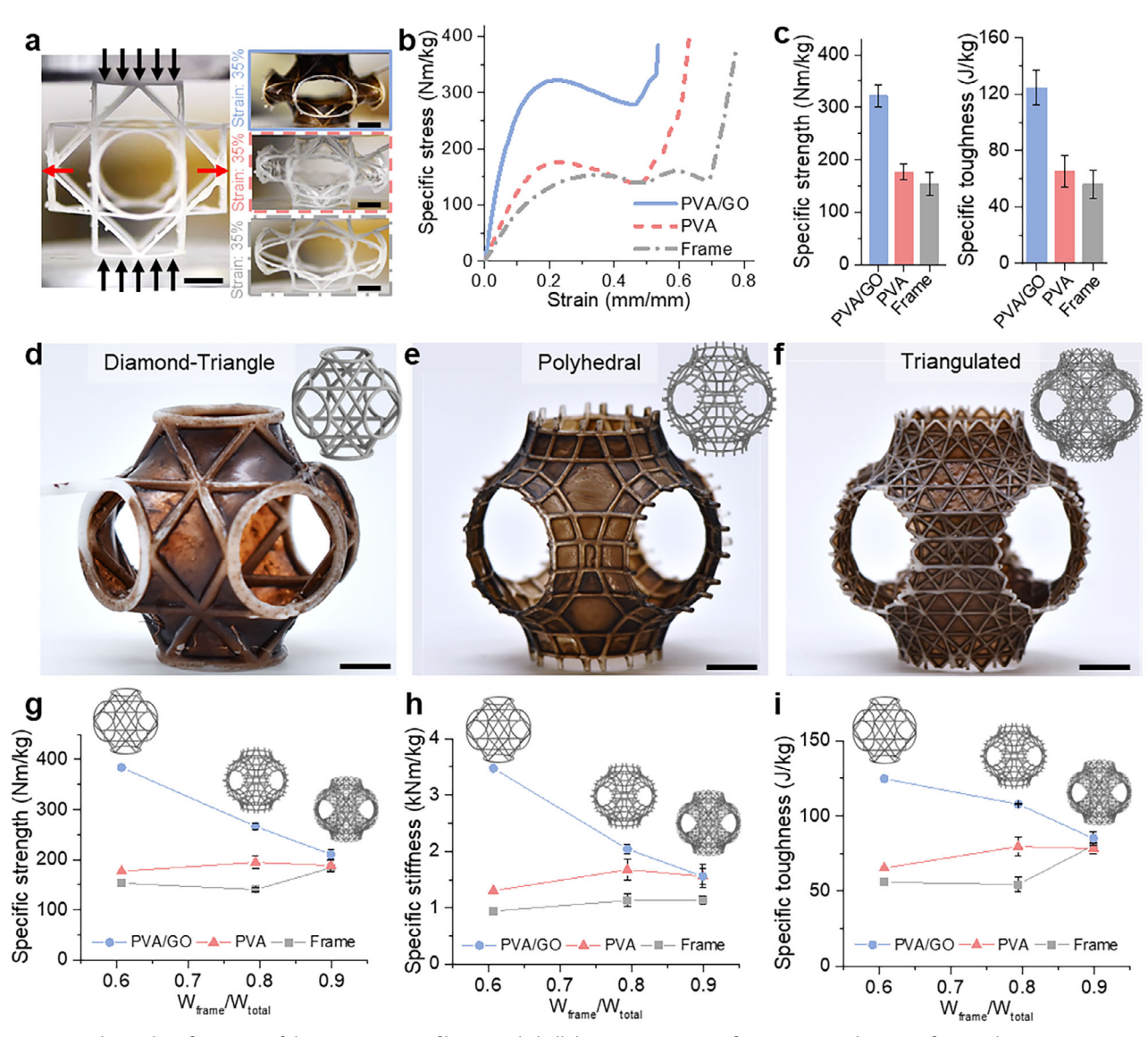


Figure 4. Mechanical performance of the PVA/GO soap film-coated shellular Primitive (P) surfaces. a) Optical image of uniaxial compression test for a strut-based P surface without the soap film coating. The structure expands laterally under vertical compression. Insets show the deformations of the PVA/GO, PVA, and uncoated P surfaces under the 35% compression strain, respectively. Scale bars: 10 mm. b) specific compressive stress (normalized by the sample weight)-strain curves for PVA/GO, PVA soap film-coated P surfaces, and bare P surface frame. c) Specific compressive strength, and toughness of PVA/GO, PVA, and uncoated P surfaces. d-f) Optical images of subdivisions: Diamond Triangle (DT) (d) polyhedral (e) and triangulated (f) of PVA/GO-coated P surfaces. The insets show the 3D models of truss-like subdivisions of P surfaces with the same density and volume ($\rho = 0.0246$ g cm⁻³, V=15.625 cm³) and are designed using Polyhedral Graphic Statics (PGS) techniques. Scale bars: 5 mm. g-i) Specific compressive strength (g), stiffness (h), and toughness (i) of PVA/GO, PVA-coated, and uncoated P surfaces of three different subdivisions. Error bars on the data show standard deviation from three independent samples. Error bars report the standard deviation from three independent samples.

of coated soap film, for different subdivisions of strut-based Psurface, we can manipulate the mechanical response of TPMS structures from strut-based frame-dominated (polyhedral and triangulated P surface) to soap-film-dominated (DT subdivided P surface). The result is further verified by tuning the strut diameter of the DT subdivided P surface (1-2 mm), where PVA/GOcoated P surfaces outperform others (Figure S10a-c, Supporting Information). Here, we also study the effect of other GObased nanocomposites coated on the DT subdivisions for generality. The results show that waterborne polyurethane (WPU)/ GO soap film-coated and gelatin/GO-coated DT subdivisions enhance more than 1 time over their counterparts (Figure \$10d,e, Supporting Information).

2.5. Impact Testing of PVA/GO P Surfaces

Next, we coat PVA/GO soap film on a 3D printed 2×2 array of DT subdivided P surface, sharing the same bulk density ($\rho =$ 0.0246 g cm^{-3} , $V = 15.625 \text{ cm}^{3}$) as the single DT subdivision (Figure 5a). The 2×2 PVA/GO soap film coated DT subdivided P surface shows enhanced specific strength (2.67 kPa m⁻³ kg⁻¹)

16163028, 0, Downloaded from https://advanced.onlinelibrary.wiley.com/doi/10.1002/adfm.202512357 by University Of Pennsylvania, Wiley Online Library on [22/09/2025]. See the Terms and Condition

anditions) on Wiley Online Library for rules of use; OA articles are governed by the applicable Creative Commons

www.afm-journal.de

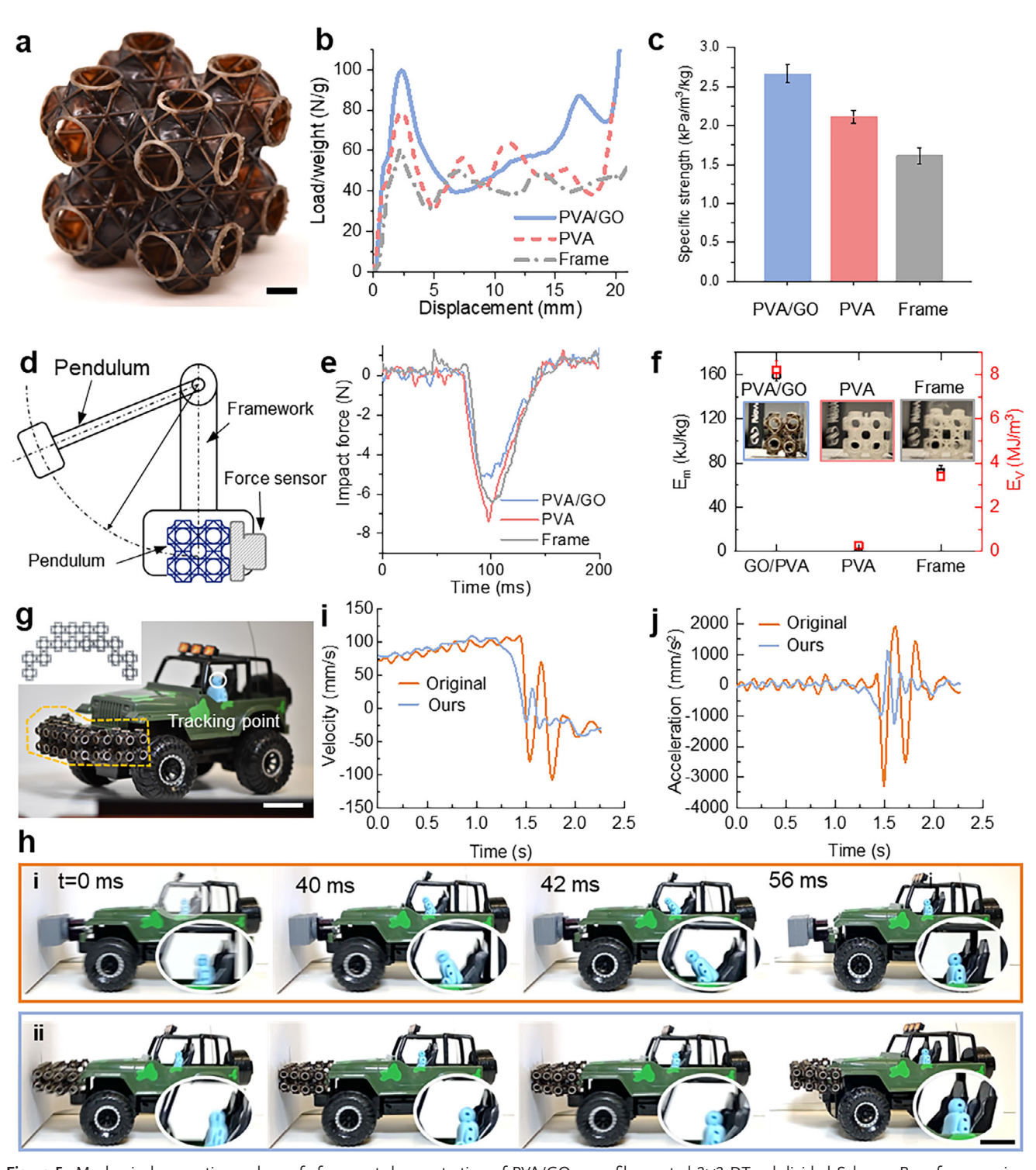


Figure 5. Mechanical properties and proof-of-concept demonstration of PVA/GO soap film-coated 2×2 DT subdivided Schwarz P surface as a jeep bumper for high specific energy absorption. a) Optical images of the PVA/GO soap film-coated P surface. Scale bar: 5 mm. b,c) Compressive load/weight-displacements curves (b) and specific compressive strength (c) for PVA/GO, PVA soap film-coated, and uncoated 2×2 P surfaces, respectively. d) Schematic of the dynamic impact test setup. e,f) Impact force-time curves (e), and normalized impact energy (f) for PVA/GO, PVA soap film-coated, and uncoated 2×2 P surfaces, respectively. Inset: the maximum deformation of three samples during the impact test. g) Photo of a scaled-down (1:24th of a real model) jeep equipped with the TPMS bumper composed of periodic DT subdivided P surfaces. The inset shows a 3D model of a truss-like TMPS bumper. The crash dummy with the motion track point on its head is deployed. Scale bar: 4 cm. h), The time-lapse side-view images of a scale-down jeep with and without the TPMS bumper during the collision tests. Scale bars: 4 cm. i,j) Comparison of tracked velocity profiles (i) and acceleration profiles (j) of the crash dummy during the collision test with and without the TPMS bumper. Error bars represent the standard deviation from three independent samples.

16163028, 0, Downloaded from https://advanced.onlinelibrary.wiley.com/doi/10.1002/adm.202512357 by University Of Pennsylvania, Wiley Online Library on [22/09/2025]. See the Terms and Conditions (https://onlinelibrary.wiley.

conditions) on Wiley Online Library for rules of use; OA articles are governed by the applicable Creative Commons

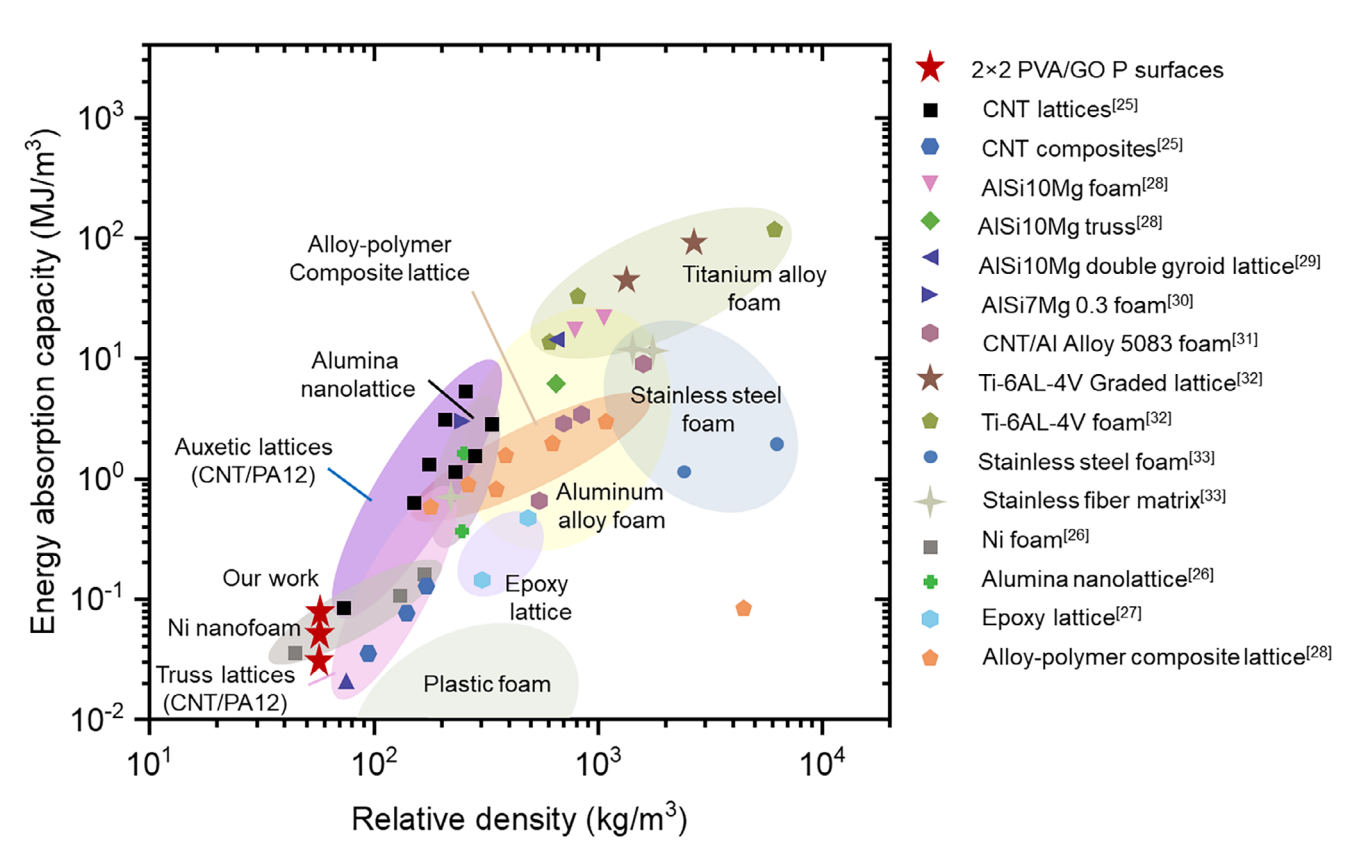


Figure 6. Ashby plot of the energy absorption per unit volume versus the relative density of different micro-/nanostructured materials.

over PVA coated (2.11 kPa m⁻³ kg⁻¹) and bare frames (1.61 kPa m⁻³ kg⁻¹) by regulating the stress and defects propagation through the aligned GO sheets compared to PVA coated and bare strut-based P surfaces (Figure 5b,c; Video S5, Supporting Information). It is important to note that since the soap films and the 3D printed wireframes are all made from brittle materials, when compressed above a certain threshold, the shellular structures fabricated here, whether soap film-coated or non-coated, experience either film and/or wireframe fracture or plastic deformation of the wireframes (Figure S11 and Video S5, Supporting Information), are thus unable to recover their original shape for cyclic loading and unloading studies. Therefore, the current shellular structures are best as single-use energy absorbers suitable for applications, such as automotive crash safety, aerospace impact mitigation, and personal protective equipment. Our preliminary results suggest that the use of thinner wireframes and elastomeric materials such as WPU as soap films could improve the elasticity, allowing the shellular structures to return to the original state. It is not clear whether any microscopic damage has occurred, though. We plan to further investigate this in the

To evaluate the energy absorption of a 2x2 PVA/GO soap filmcoated DT subdivided P surface, we built an impact tester with a pendulum designed to deliver a controlled impact force to the specimen (Figure 5d; Figure S12, Supporting Information). The reduced force relayed from the PVA/GO-coated P surface compared to the PVA-coated and bare frame, P surface reveals that the PVA/GO-coated one absorbs energy from dynamic impacts through elastic collapse under the extreme compression condition (Figure 5e; Video S6, Supporting Information). The impact energy can be effectively guided and dissipated through the anisotropic alignment of GO sheets within the shellular enlarged surface area. The absorbed energy is normalized by the total mass and volume, showing that the PVA/GO soap film-coated P surface offers exceptional energy absorption capability, 1.5963 kJ kg^{-1} or 0.0821 MJ m^{-3} , vs. those of PVA-coated P surface, 0.0495 kJ kg⁻¹ or 0.0027 MJ m⁻³, and those of the bare wireframe, $0.06483 \text{ kJ kg}^{-1}$ or 0.0340 MJ m^{-3} , respectively (Figure 5f). To examine the effect of the strain rate on impact performance, we adjust the pendulum release height (H) in our scaled-down impact test setup. This allows us to vary the impact velocity and correspondingly the strain rate (Table S1, Supporting Information). As shown in Figure S13 (Supporting Information), when the pendulum was dropped at H = 60 mm, the PVA/GO soap film-coated P surface absorbed four times more impact energy per volume compared to that dropped at H = 20 mm. This indicates that higher impact strain rates associated with greater release heights lead to increased peak impact forces and higher specific energy absorption. These results highlight the strain-ratesensitive energy dissipation behavior of the shellular structure.

To benchmark our design vs. the existing energyabsorbing materials, we compare the specific energy absorption performance of our 2×2 PVA/GO-coated P surfaces with various lightweight architected materials reported in literature in an Ashby plot (Figure 6), including CNT lattices, [25] nickel nanofoams, [26] epoxy lattices, [27] alloy-polymer





www.afm-journal.de

composite lattice, [28,29] alumina nanolattice [30] and titanium alloy foams and lattices, [31,32] and stainless steel foams and fiber matrix. [33] Remarkably, our structure, while using a polymerbased lattice framework, achieves a lower relative density than the polymer foams and CNT lattices, while maintaining comparable or superior specific energy absorption capacity. This demonstrates that our ultrathin soap film-coated shellular surfaces, which combine the low density and high energy absorption performance, offer a compelling strategy for lightweight impact protection applications. Compared with more complex or resource-intensive fabrication methods such as Electron Beam Melting (EBM) or Selective Laser Melting (SLM), our approach is simple, scalable, low-cost, and modulable at the macroscopic level.

Lastly, as a proof-of-concept demonstration, we fabricate a PVA/GO soap film-coated P surface as a jeep bumper composed of DT subdivision as the unit cell (Figure 5g). The collision tests are performed using a scaled-down jeep model (1/24th of the actual size) to evaluate whether the bumper can absorb kinetic energy and imitate inertia at the instantaneous velocity ≈100 mm s⁻¹. A crash test dummy is employed, and the motion of its head is tracked throughout the collision. Since the bumper, composed of the subdivided P surfaces, absorbs the impact energy and prolongs the collision process, the dummy maintains a stable position with minimal oscillation (Figure 5h(i); Video \$7, Supporting Information). We further dismantle the PVA/GOcoated bumper to check its mechanical integrity and find no obvious damage. In contrast, severe vibration happens to the dummy sitting in the jeep with its original bumper during the collision (Figure 5h(ii)). By tracking the motion of the dummy's head during the collision, we reveal that the velocity and acceleration of the jeep with the shellular bumper can be reduced by 66% and 61%, respectively, suggesting that the shellular bumper can effectively absorb kinetic energy and reduce the force transmitted to the vehicle and the occupants. Although the vehicle collision velocity is slower than the actual one, which requires special equipment to generate, the preliminary results are encouraging.

3. Conclusion

In conclusion, we fabricate shellular TPMS structures with a thin continuous shell of LLC GO/PVA through a one-step, defecttolerant dip coating method. The curvature and orientation of the soap films are regulated by the surface tension to reach the minimal energy state. GO nanosheets are oriented as regulated by the geometry of the template, driven by the gradient of evaporation rate during the liquid-to-solid phase transition. The resulting PVA/GO soap film-coated shellular TPMS structures show exceptional stiffness, strength, toughness, and energy absorption capability, yet are lightweight. Our strategy provides a platform to create metamaterial structures with minimal surfaces and thin curved shells. The study of the correlation between the geometry-anisotropy, phase-transition, and the underlying physicochemical properties will inspire the creation of a wide range of composites, e.g., hydrophilic polymers mixed with nanofillers, and across the scales for potential applications, including shape-morphing,[34] building envelopes,[35] personal protection, [36,37] energy storage, [17] and tissue engineering. [38]

4. Experimental Section

Materials: Poly(vinyl alcohol) (PVA) with a weight-average molecular weight (M_W) of 1 25 000 g mol $^{-1}$, gelatin from porcine skin, and waterborne polyurethane (WPU) were purchased from Sigma–Aldrich. Graphene oxide (GO) dispersion (20 mg mL $^{-1}$ in water, lateral size 2–4 μ m) was purchased from Ceylon Graphene Technologies, Sri Lanka. Sodium chloride (ACS reagent >99%), lithium chloride (ACS reagent >99%), potassium carbonate (reagent grade >98%), and sodium sulfate (ACS reagent >99%, anhydrous, granular) were purchased from Sigma–Aldrich. Isopropyl alcohol (IPA) (70% v/v) and sulfuric acid (95%-98% w/w certified ACS plus) were purchased from Fisher Scientific. UV curable White Model Resin for 3D printing was purchased from HARZ Labs LLC. The plastic balloon was purchased from Amazon (magic bubble) and made from poly(vinyl acetate) (PVAc). The bowling ball (7 kg) was purchased from Brunswick TZone Deep Space.

3D Printing of the Strut-Based Frames as Templates for Soap Film Coating: All strut-based frames were 3D printed using a Phrozen Mini 4K digital light processing (DLP) 3D printer using UV-curable methacrylate monomer and oligomer-based HARZ Labs white model resin. The 3D models for printing were sliced to 50 μm layers in Chitubox software, and the curing time for each layer was set to 8 s with a 20 s light-off delay. After each layer was cured, the build plate was lifted for 5 mm at 65 mm min $^{-1}$ before returning to the position to cure the next layer. Immediately after the print, the build plate attached to the printed model was immersed in an isopropyl alcohol (IPA) bath and sonicated for 10 min in a Branson 3800 Ultrasonic cleaner to remove uncured resin, followed by air drying and 405 nm flood UV exposure to completely crosslink the resin. The dimension of all single and 2 \times 2 Schwarz-P surfaces was kept at 25 mm \times 25 mm.

Preparation of the Polymer/GO Soap Films: The PVA aqueous solutions and 10wt.% were prepared by mixing PVA in desired amounts of deionized (DI) water in glass beakers. The mixture was magnetically stirred in an 80 °C oil bath on a hotplate (IKA C-MAG HS 7) till it became homogeneous. The solution was completely cooled down to room temperature before use. PVA/GO mixture was formulated by mixing 10 wt.% PVA aqueous solution with 20 mg mL⁻¹ GO water dispersion, followed by vortexing using the Fisher Scientific Heavy-Duty Microplate Vortex Mixer till forming a homogeneous solution. The weight ratio of PVA: GO was fixed at 10:1, with a total mass concentration of the mixture of 50 mg mL⁻¹. Before the fabrication of the soap film, 3D printed strut-based frames were oxygen plasma treated (Harrick Scientific Corp PDC-001 plasma cleaner/sterilizer. The mass of the empty frame was recorded on a balance (Sartorius Entris224I-1S) before dipping it into the solution. After dipping, the excess solution on the frame was wiped off, and the mass suspended on the frame was controlled by adding or subtracting using a clean tweezer, followed by weighing repeatedly until reaching the desired weight. Then, the frame was immediately fixed on polystyrene foam, and the entire setup was placed in a closed, home-built glass chamber with controlled RH for drying. The RH inside the chamber (10-90%) was controlled using an open glass petri dish filled with sulfuric acid or aqueous saturated salt solutions. A closed chamber with concentrated sulfuric acid (98 wt.%) and saturated LiCl aqueous solution had RH of 10 % and 20%, respectively, and that from saturated K2CO3, NaCl, and Na2SO4 aqueous solutions had RH of 50%, 75%, and 90%, respectively. The RH in the chamber was allowed to stabilize for at least 12 h before use and was continuously recorded by a humidity monitor (Habor HM118A) during the soap film drying. After drying, the mass of the soap film-coated structure was recorded. The cast film was conducted by depositing the liquid solution onto the glass substrate, using a home-made blade casting device to uniformly spread it across the surface. The film's thickness was controlled by adjusting the blade's height and spreading speed. After fully drying, the cast film was cut to the same dimensions as the soap film for the uniaxial tensile test.

Gelatin soap solution was formulated by adding 3g gelatin powder into a beaker, followed by the addition of 3g DI water. Subsequently, 24 g 80 °C DI water was added and the beaker was heated in 80 °C oil bath and magnetically stirred on a hotplate (IKA C-MAG HS 7) until a clear solution was



www.afm-journal.de

obtained. Gelatin soap film was prepared following similar procedures to fabricating the PVA soap films.

Gelatin/GO soap solution was formulated by mixing the above gelatin aqueous solution (10 wt.%) with 20 mg mL $^{-1}$ GO aqueous dispersion at 80 °C, followed by vortexing. The weight ratio of gelatin: GO was fixed at 10:1, with a total mass concentration of the mixture at 50 mg mL $^{-1}$. Before coating, the physical gel was heated on a 50 °C hotplate until melted. Treatment of the template, step for dipping, mass control, and drying were identical to those for PVA soap film.

The WPU and WPU/GO soap films were prepared following the same procedures as preparing the PVA and PVA/GO soap films. WPU/GO soap solution was formulated by mixing WPU with 20 mg mL $^{-1}$ GO aqueous dispersion at 80 °C, followed by vortexing until a homogeneous solution was formed. The weight ratio of WPU:GO was fixed at 10:1, with a total mass concentration of 50 mg L $^{-1}$.

Material Characterization: The morphologies of GO nanosheets were characterized by FEI Quanta 600 environmental scanning electron microscopy (ESEM) with an electron beam acceleration voltage of 10 kV under 0.50 Torr.

The polarized optical microscopy (POM) images were recorded on a home-built set-up, including a white light source (Motic MLC-150C fiber optic illuminator), a linear polarizer (Thermo Fisher Scientific), a rotatable sample holder (Thermo Fisher Scientific), a rotatable waveplate holder (Thermo Fisher Scientific LCC1223-A), an analyzer with optical axis perpendicular to that of the polarizer (Thermo Fisher Scientific), and a digital camera, aligned on the same optical path (see setup shown in Figure S4, Supporting Information).

Dynamic light scattering (DLS) was performed on Zetasizer (Malvern nano-s dynamic light scattering particle size analyzer) to estimate the size distribution of graphene oxide sheets dispersed in DI water.

Atomic force microscopy (AFM, Asylum MFP-3D) was applied to study the morphology of the PVA/GO soap films and GO sheets, wherein two tapping mode AFM probes, TESPA-V2 and HQ:NSC15/Al BS, were selected for the mapping, respectively. In a typical AFM mapping process, the sample was placed on a polished silicon wafer. The AFM tip was moved to the targeted air with the assistance of an optical microscope, and the tomography mapping was conducted in AC mode in the air.

Polarized Raman spectroscopy was employed to study the orientation of the GO nanosheets in the PVA/GO soap films. A 532 nm laser was equipped, and the laser spot diameter was regulated to around 1 μm . For the polarization measurement, first, the PVA/GO soap film was placed onto a silicon wafer with the laser beam perpendicular to the sample's surface. While the sample was fixed, the polarized angle of the laser beam was continuously rotated using a half-wave plate to attain the spectra. To measure the transverse section of the thin film, the sample was fixed using a self-closing tweezer. The relative intensities of the G band at 1598 cm $^{-1}$ were recorded.

Mechanical Testing: The tensile and compressive tests were conducted using a universal mechanical tester (Instron 5564) with a stretching speed of 2 mm min⁻¹ and a compression speed of 7.5 , respectively. The custom setup for the dynamic impact test of soap film-coated TPMS structures (Figure \$12, Supporting Information) was adapted from the Charpy impact test, following the same principle of the standardized method (ASTM E23, ISO 148) for evaluating the energy absorption capacity of materials under high-strain-rate conditions. Ours was scaled down to accommodate the centimeter-sized, ultralightweight shellular structures in the system. Specifically, it consisted of a framework (Thorlabs), a pendulum (265 g, 160 mm in length, Thorlabs) suspended from the framework, and a force sensor (Instron, Serial Number: 41993, 2 kN) to measure the impact load. The specimen was positioned horizontally on the framework between the pendulum and the impact force sensor. The pendulum was released from a specific height H to impact the specimen.

The effective stroke displacement S_{ef} , mass of the P surface m, and the stroke load F are employed to describe the mechanical response of

the P surface under an impact load. The specific energy absorption SEA is defined as $^{[39,40]}$

$$SEA = \frac{EA}{m} \tag{1}$$

where EA is the total energy absorption, defined as

$$EA = \int_{0}^{S_{ef}} F du$$
 (2)

The Frontal Collision Test of a Vehicle: The crash dummy (0.38 g) made from air-dry clay (FlyFlag) was placed into a remote-controlled vehicle (TEMU). A PVA/soap film-coated TPMS bumper was attached to the front of the vehicle. The dummy's head motion was marked and tracked during the collision. The vehicle's speed was maintained at 100 mm s $^{-1}$ before impacting the frontal obstacle. All videos were captured using a Nikon D5600 DSLR, and the motion analysis was conducted using Tracker software.

Finite Element Analysis (FEA): FEA simulations were conducted using Abaqus/Standard (Dassault Systèmes) to model the stress development during the solid-to-liquid phase transition in templated PVA/GO soap films. The geometry of triangular films (l = 10 mm), identical to the experimental setup, was imported into ABAQUS CAE as a STEP file and meshed using 4-node tetrahedral elements (C3D4). A mesh refinement study was performed to ensure mesh accuracy. The mechanical properties of PVA/GO were modeled as linear elastic with a constant Young's Modulus of 10 kPa and a Poisson's ratio of 0.3. To simulate compression during the drying process, the isotropic thermal expansion coefficient of thermal expansion was set to -0.2 °C⁻¹. Boundaries were fully constrained at the edges to replicate the constraints provided by the strut-based frame. A static simulation was performed, with the temperature increased to simulate the compression during the evaporation. The orientations of the principal stress (indicated by light blue lines) were plotted to show that the direction of GO sheet alignment was normal to the direction of maximum principal stress.

Static Analysis: Raw data were processed and plotted in MATLAB to calculate the mean and standard deviation (SD). The results were presented as mean \pm SD. Each statistical analysis was performed with a sample size n=3.

Supporting Information

Supporting Information is available from the Wiley Online Library or from the author.

Acknowledgements

Arjun Kanthawar, Julian Samek, Viraat Singh, Aidan Young, and Desmond Young are acknowledged for early studies, showing the potential of the shellular structures in their senior design project under the supervision and guidance by S.Y. The authors also acknowledge the discussions with Dr. Pierre-Thomas Brun (Princeton University). The research is supported by National Science Foundation (NSF) Future Eco Manufacturing Research Grant (FMRG, # CMMI 2037097, to S.Y. and M.A.). K-Y.W. acknowledges the support from Vagelos Institute of Energy Science and Technology (VIEST) Postdoctoral Fellowship.

Conflict of Interest

The authors declare no conflict of interest.

Author Contributions

Y.C. and Y.G. contributed equally to this work. Y.C., Y.G., and S.Y. conceived the concept. Y.C., Y.G., and M.P. fabricated the PVA/GO soap film-coated

of use; OA

are governed by the applicable Creative Commons

www.advancedsciencenews.com



www.afm-journal.de

structures. Y.C., Y.G., K-H.Y., K-Y.W., S.F., and Z.Z. characterized samples. M.A. and M.A. designed the subdivisions of the strut-based Schwarz-P surface. Y.C. performed finite element analysis. Y.C. and K-H.Y. analyzed the experimental data. S.Y. supervised the project. Y.C., Y.G., and S.Y. wrote the manuscript. All authors provided feedback and contributed to the manuscript.

Data Availability Statement

The data that support the findings of this study are available in the supplementary material of this article.

Keywords

energy absorption, high strength-to-weight ratio, lyotropic liquid crystalline graphene oxide, primitive triply periodic minimal surface, soap films

Received: May 16, 2025 Revised: July 31, 2025 Published online:

- Q. Li, J. Kulikowski, D. Doan, O. A. Tertuliano, C. J. Zeman IV, M. M. Wang, G. C. Schatz, X. W. Gu, Science 2022, 378, 768.
- [2] X. Zhang, A. Vyatskikh, H. Gao, J. R. Greer, X. Li, Proc. Nat. Acad. Sci. USA 2019, 116, 6665.
- [3] S. Dickson, Mathematica J. 1990, 1, 38.
- [4] C. Isenberg, The Science of Soap Films and Soap Bubbles, Dover Publications, New York 1992.
- [5] S. Zhou, Y. Zhao, K. Zhang, Y. Xun, X. Tao, W. Yan, W. Zhai, J. Ding, Nat. Commun. 2024, 15, 6481.
- [6] J. Shi, H. Mofatteh, A. Mirabolghasemi, G. Desharnais, A. Akbarzadeh, Adv. Mater. 2021, 33, 2102423.
- [7] M. Akbari, A. Mirabolghasemi, M. Bolhassani, A. Akbarzadeh, M. Akbarzadeh, Adv. Funct. Mater. 2022, 32, 2109725.
- [8] X. Zheng, W. Smith, J. Jackson, B. Moran, H. Cui, D. Chen, J. Ye, N. Fang, N. Rodriguez, T. Weisgraber, Nat. Mater. 2016, 15, 1100.
- [9] X. Zheng, H. Lee, T. H. Weisgraber, M. Shusteff, J. DeOtte, E. B. Duoss, J. D. Kuntz, M. M. Biener, Q. Ge, J. A. Jackson, S. O. Kucheyev, N. X. Fang, C. M. Spadaccini, *Science* 2014, 344, 1373.
- [10] A. E. Aliev, J. Oh, M. E. Kozlov, A. A. Kuznetsov, S. Fang, A. F. Fonseca, R. Ovalle, M. D. Lima, M. H. Haque, Y. N. Gartstein, M. Zhang, A. A. Zakhidov, R. H. Baughman, *Science* 2009, 323, 1575.
- [11] X. Yu, H. Cheng, M. Zhang, Y. Zhao, L. Qu, G. Shi, Nat. Rev. Mater. 2017, 2, 17046.

- [12] T. Kato, Y. Hirai, S. Nakaso, M. Moriyama, Chem. Soc. Rev. 2007, 36, 1857.
- [13] Y. Gao, J. Liu, S. Yang, Mater. Today 2023, 69, 19.
- [14] R. Narayan, J. E. Kim, J. Y. Kim, K. E. Lee, S. O. Kim, Adv. Mater. 2016, 28, 3045.
- [15] B. Wang, S. Mukataka, E. Kokufuta, M. Ogiso, M. Kodama, J. Polym. Sci. B 2000, 38, 214.
- [16] J. Kim, G. Zhang, M. Shi, Z. Suo, Science 2021, 374, 212.
- [17] Y. Xia, T. S. Mathis, M.-Q. Zhao, B. Anasori, A. Dang, Z. Zhou, H. Cho, Y. Gogotsi, S. Yang, *Nature* 2018, 557, 409.
- [18] C. Bao, Y. Guo, L. Song, Y. Hu, J. Mater. Chem. 2011, 21, 13942.
- [19] A. A. Evans, E. Cheung, K. D. Nyberg, A. C. Rowat, Soft Matter 2017, 13, 1056.
- [20] Y. Gao, Y. Chi, M. Patel, L. Jin, J. Liu, P.-T. Brun, S. Yang, arXiv 2025, arXiv:2503.06065.
- [21] Z. Li, R. J. Young, N. R. Wilson, I. A. Kinloch, C. Vallés, Z. Li, Comp. Sci. Technol. 2016, 123, 125.
- [22] L. Liu, J. Zhang, J. Zhao, F. Liu, Nanoscale 2012, 4, 5910.
- [23] Z. Wang, X. Shen, M. Akbari Garakani, X. Lin, Y. Wu, X. Liu, X. Sun, J.-K. Kim, ACS Appl. Mater. Interfaces 2015, 7, 5538.
- [24] M. Ross, Diff. Geom. Appl. 1992, 2, 179.
- [25] S. Yuan, C. K. Chua, K. Zhou, Adv. Mater. Technol. 2019, 4, 1800419.
- [26] S.-f. Fan, T. Zhang, K. Yu, H.-j. Fang, H.-q. Xiong, Y.-l. Dai, J.-j. Ma, D.-y. Jiang, H.-l. Zhu, Trans. Nonferrous Metals Soc. China 2017, 27, 117.
- [27] J. Mueller, J. R. Raney, K. Shea, J. A. Lewis, Adv. Mater. 2018, 30, 1705001.
- [28] L. Stanev, M. Kolev, L. Drenchev, B. Krastev, J. Mater. Eng. Perform. 2020, 29, 3767.
- [29] I. Maskery, N. Aboulkhair, A. Aremu, C. Tuck, I. Ashcroft, R. D. Wildman, R. Hague, Mater. Sci. Eng. A 2016, 670, 264.
- [30] F. Ning, W. Cong, Y. Hu, H. Wang, J. Composite Mater. 2017, 51, 451.
- [31] J. H. Martin, B. D. Yahata, J. M. Hundley, J. A. Mayer, T. A. Schaedler, T. M. Pollock, *Nature* 2017, 549, 365.
- [32] H. Rafi, N. Karthik, H. Gong, T. L. Starr, B. E. Stucker, J. Mater. Eng. Perform. 2013, 22, 3872.
- [33] Y. Alvandi-Tabrizi, A. Rabiei, Procedia Mater. Sci. 2014, 4, 377.
- [34] K. Oliver, A. Seddon, R. S. Trask, J. Mater. Sci. 2016, 51, 10663.
- [35] Y. Li, Y. Zhao, Y. Chi, Y. Hong, J. Yin, Mater. Today Energy 2021, 22, 100874.
- [36] D. Tahir, M. Zhang, H. Hu, Phys. Status Solidi B 2022, 259, 2200324.
- [37] L. Jin, M. Yeager, Y.-J. Lee, D. J. O'Brien, S. Yang, Sci. Adv. 2022, 8, aba3248.
- [38] G. Lu, Y. Xu, Q. Liu, M. Chen, H. Sun, P. Wang, X. Li, Y. Wang, X. Li, X. Hui, Nat. Commun. 2022, 13, 2499.
- [39] W. Yang, B. Peng, K. Yang, Compos. Struct. 2025, 356, 118865.
- [40] K. Yang, W. Yang, S. Duan, W. Yang, Y. Lin, Eng. Struct. 2025, 322, 119154.